Insight into the Dependence of Photovoltaic Performance on Interfacial Energy Alignment in Solar Cells with Mobile Ions

Matías Córdoba and Kurt Taretto*

A key aspect in the optimization of perovskite (PVK) solar cells is the mitigation of interface losses, which are determined by energy band offsets and recombination. Counterintuitively, recent experimental evidence on inorganic PVK solar cells shows that increasing band offsets may improve open-circuit voltage at efficiency levels over 20%. In order to improve the knowledge of the impact of interfaces, the authors model solar cells consisting of an intrinsic absorber material containing mobile ions, sandwiched between two wide-gap charge transport layers. The results show that minimizing band offsets decreases interface losses in various scenarios, but cannot be adopted as a universal optimization rule. For instance, even in the absence of interface recombination, unequal majority carrier band offsets avoid high injection conditions. Moreover, assuming a fixed band offset at one interface, the band offset at the opposite interface should be reduced if it shows the highest interface recombination, or increased if it shows the lowest recombination. Remarkably, it is found that solar cells with mobile ions hold the potential to outperform of ion-free counterparts, depending on the extent to which the interplay between band offsets and Debye layers result in the establishment of a majority carrier concentration in the intrinsic absorber.

1. Introduction

In the last 10 years, perovskite (PVK) materials prepared with earth-abundant elements and high-vacuum independent methods rapidly emerged as the landmark material for cutting edge photovoltaics.[1] Based on an exceptionally high absorption coefficient and low defect concentrations, sub-micron thick PVK absorbers readily deliver solar cells with laboratory scale conversion efficiencies comparable to mainstream silicon solar cells.[2] Having reached high bulk optoelectronic quality with several PVK formulations and most film preparation methods, the focus

on the efficiency improvement of PVK solar cells promptly shifted from the bulk to the interfaces.[3–6] Interface losses arise mainly from energy losses due to band offsets between the charge transport layers (CTLs) and the PVK, and recombination of photogenerated carriers via interface defects. The efforts were directed in different directions: early experimental work identified energy barriers for carriers extraction[3,7] and experimental routes to avoid them,[8] later contributions focused in interface defect passivation to mitigate recombination,[4] or in reducing band offsets by changing the work function of the CTLs.[9] Further studies systematized interface modification as well as characterization techniques,[10–14] recognizing the necessity of finding better-suited interface characterization methods.[15,16]

The bottleneck for further optimization of PVK solar cells appears to be the refinement of the choice of appropriate CTL materials producing low band offsets, or the addition of interlayers capable of passivating interface recombination. However, this problem unfolds a high complexity due to several aspects. First, there is an exceptionally vast choice of suitable CTL materials, covering organic as well as inorganic compounds.[17–20] In order to bypass the difficulty to test the very large number of candidate CTL materials, a better-founded approach is required. As recently stated by Siekman et al., "to avoid having to choose randomly and to perform a trial-and-error based optimization, gaining insights into the effect of charge-transport layers on the performance, recombination and charge collection in perovskite solar cells is of critical importance".[21] Second, a reassessment of the influence of energy alignment turns mandatory due to the variety of experimental results, which are sometimes contradictory between different laboratories.[15] For instance, recent experiments with inorganic PVK solar cells provide seemingly counter-intuitive evidence for the behavior of interface energy offsets, as higher band offsets for majority carriers were shown to improve all solar cell output parameters.[22] Other studies confirm the generally accepted rule of lowering band offsets,[23] however rising fundamental questions: in metalorganic PVK solar cells, Haddad et al. correlated small band offsets with smaller interface recombination, yet observing that recombination at the PVK/fullerene interface was partly determined by the choice of the opposite CTL material and the underlying substrate.[5] This finding is

M. Córdoba, K. Taretto
Dto. de Electrotecnia
Fac. de Ingeniería (UNCo)
Buenos Aires 1400, 8300 Neuquén, Argentina
E-mail: kurt.taretto@fain.uncoma.edu.ar

K. Taretto
Inst. de Investigación y Desarrollo en Ingeniería de Procesos
Biotecnología y Energías Alternativas (PROBIEN, CONICET-UNCo)
Buenos Aires 1400, 8300 Neuquén, Argentina

ⓘ The ORCID identification number(s) for the author(s) of this article can be found under https://doi.org/10.1002/solr.202300742.

again counter-intuitive, as it prompts the fundamental question of how one interface can impact recombination at the opposite interface.

In order to shed some light into the intricacies of interface recombination in solar cells with mobile ions, modeling studies focused on the effect of interface energy offsets either neglecting[24] or including ions.[25,26] Recent numerical simulations in PVK solar cells by Mozafari et al. have indicated that the inclusion of ions is essential,[25] demonstrating that ion accumulation at the interfaces manipulates recombination via interface potentials. Although very scarce, earlier experimental reports also supported the hypothesis of mobile ions directly influencing recombination in PVK solar cells.[27]

In this work, we specifically focus on the validity of the (often understood as intuitive) rule of minimizing majority carrier band offsets to improve efficiency. To this end, we model solar cells assuming high quality material parameters which nominally enable high efficiencies, in two extreme cases: very high and zero mobile ion concentration. We find that with high mobile ion concentrations in the absorber, reducing band offsets not necessarily provides better performance. Moreover, the choice of appropriate CTLs does not only affect interface losses: even without interface recombination, band offsets significantly affect bulk recombination. These findings are aided by analytical expressions for the open-circuit voltage, which help rationalize the differences between cells with and without mobile ions. Starting with the fundamentals, Section 2 of this article provides definitions and band-diagrams for ion-free as well as mobile ion-rich solar cells, together with the recombination equations for bulk and interface recombination. Section 3 gives the derivation of analytical expressions for the open-circuit voltage as a function of interface energy offsets and band bendings, and presents the numerical model. Section 4 presents the results obtained from the analytical and numerical models, discussing the stark contrasts between cells without and with mobile ions. In Section 5 we discuss the results from a more general technological point of view, drawing conclusions.

2. Fundamentals

2.1. Energy Bands and Potentials

Figure 1a shows the energy band diagrams of three isolated semiconductors required for the studied solar cell: a high bandgap electron transport layer (ETL), an absorber layer with lower bandgap E_g (in our case a perovskite), and a high bandgap hole transport layer (HTL). In the following, we may refer indistinctly to the ETL or HTL as CTLs. Upon junction of the layers, band offsets between ETL/absorber and absorber/HTL appear whenever there are differences between the electron affinities $q\chi_i$ and the energy gap of the implied materials. Within this work, the relevant offsets are majority carrier band offsets: the conduction band offset ΔE_C at the ETL/absorber interface, and the valence band offset ΔE_V at the absorber/HTL, as indicated in Figure 1a. Minority carrier offsets are assumed to sufficiently high as to impose an energy barrier that completely prevents minority carriers to enter the CTLs, i.e., not presenting any loss to photocarrier collection.

Upon photovoltaic action, electrons (blue dot in Figure 1a) are required to sweep from the absorber to the ETL and further to the contacts (not shown), while holes (red dot) sweep to right towards the HTL and the opposite contact. In order to enable high photocurrents, it is mandatory that the band offsets do not pose any energy barrier to the carriers, and facilitate the extraction of carriers from the absorber. Therefore, the conditions $\Delta E_C \geq 0$ and $\Delta E_V \geq 0$ are ideally sought for in efficient designs; the positive directions being indicated in Figure 1a for each band offset. Once within the CTLs, the carriers flow towards the outward contacts (not shown in Figure 1a). In order to facilitate this task, the ETL is an *n*-type semiconductor, while the HTL is *p*-type. This shifts the equilibrium Fermi levels of the CTLs away from the bandgap center, defining the activation energies $q\xi_n$, $q\xi_p$ shown in Figure 1a.

Upon junction formation, the three layers in Figure 1a form a single stack, and the differences in work functions and Fermi levels derive in an electrostatic rearrangement and a built-in potential V_{bi}. Figure 1b,c display two possible energy band diagrams, representing extreme cases for the location of the built-in potential: (b) neutral interfaces, where V_{bi} falls completely within the absorber, and (c) highly charged interfaces, where V_{bi} falls in a distributed manner at the interfaces, via the band bendings $q V_{1-4}$. The junction with neutral interfaces (b) appears in well-behaved inorganic semiconductors without charged interfacial defects states, resulting in an ideal nip (or pin) structure. The junction with charged interfaces (c) occurs in highly defective
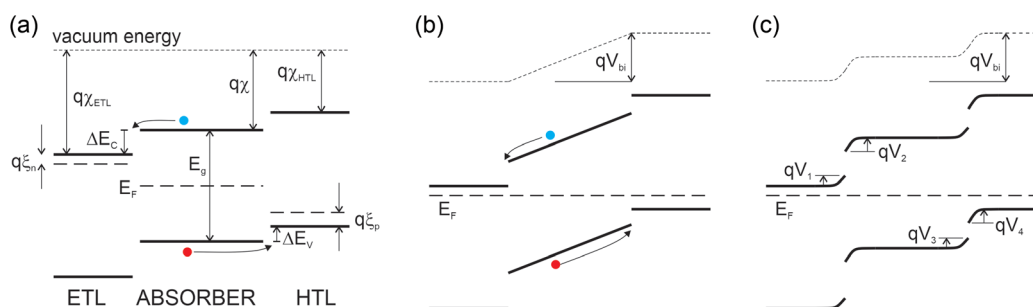

Figure 1. a) Individual energy band diagrams for the three layers of a solar cell based on a central semiconductor as absorber layer, an electron transport layer (ETL) and a hole transport layer (HTL). b,c) Junction of the three layers: in thermodynamic equilibrium the Fermi level E_F is the same throughout the structure, implying the appearance of energy band adjustments. Without any interface charges we have diagram (b), while (c) shows the opposite extreme of highly charged interfaces. Both structures have the same built-in voltage V_{bi}: in structure (b) V_{bi} falls within the central semiconductor (absorber), and in (c), V_{bi} is the sum of the four interface potential drops V_{1-4}.

interfaces, or, when the absorber semiconductor contains mobile ionic species, such as PVKs, in which case the interfaces are termed Debye layers. Since we are interested in the latter case, we term the structure of Figure 1c as the "ionic solar cell".

Regardless of the type of resulting band diagram, the built-in potential of the solar cell is given by the work function difference between the ETL and the HTL according to

$$qV_{bi} = (q\chi_{HTL} + E_{g,HTL} - q\xi_p) - q(\chi_{ETL} + \xi_n) \tag{1}$$

where $E_{g,HTL}$ is the bandgap of the HTL. Following Figure 1a, we may rewrite the built-in potential in terms of the band offsets, obtaining

$$qV_{bi} = E_g - \Delta E_C - \Delta E_V - q\xi_n - q\xi_p \tag{2}$$

which shows the built-in voltage decreasing linearly with increasing band offsets.

Turning to the ionic solar cell, the formation of the band diagram with the occurrence of interface potential drops is well described by different models.[28] The case of Figure 1c, showing flat energy bands in the interior of the absorber is valid when the mobile ions are sufficient to shield any electric field from the interior of the absorber. Thus, the built-in voltage is completely accommodated by the interface potential drops, and, in the general situation of a steady-state externally applied potential V, the sum of the interface potentials must equal the net applied potential $V_{bi} - V$, i.e.,[29]

$$V_{bi} - V = V_1 + V_2 + V_3 + V_4 \tag{3}$$

with positive bias corresponding to $V > 0$. The values V_{1-4} are related to the surface charge density Q_{Debye} induced by ionic displacement towards the interfaces. Assuming an intrinsic absorber, the dependence $V_{1-4}(Q_{Debye})$ is given by the ion concentrations, the dielectric constants in the different layers, and the doping concentrations in the CTLs.[30] In the most simple formulation for the ionic solar cell, two ionic species of opposite charge are considered: immobile anions with concentration N_0, and mobile cations with identical average concentration, and local concentration P. Notice that since the cations are partly accumulated at the narrow Debye layers, the average cation concentration remaining in the bulk is given by

$$P_{bulk} = N_0 - |Q_{Debye}|/qd \tag{4}$$

Where d is the absorber thickness. Moreover, in the specific case of metal halide PVK in combination with commonly used CTL materials,[31] the higher dielectric constant of the PVK[32] implies that most of the band bending occurs at the CTLs, i.e., $(V_1, V_4) > (V_2, V_3)$, yielding

$$V_{bi} - V \simeq V_1 + V_4 \tag{5}$$

Under illumination conditions, and at the open-circuit voltage, this expression holds provided the photogenerated charge carrier concentrations are much smaller than the ion concentrations.

The open-circuit voltage is understood as the difference between free energies of carriers at each contact. Since the free energy corresponds to the majority carrier quasi-Fermi level (QFL),[33] the open-circuit voltage V_{OC} is given by

$$qV_{OC} = E_{Fn}(\text{left}) - E_{Fp}(\text{right}) \tag{6}$$

Where E_{Fn} and E_{Fp} are the electron and hole QFLs, respectively. Here, left and right correspond to the outmost positions of the ETL and the HTL, respectively, as in Figure 1 (see Supporting Information for additional comments on the QFLs).

When considering Equation (3) under illumination and open-circuit conditions, the open-circuit voltage may lead to negative interface potentials if $V_{bi} < V_{OC}$. The high values of V_{OC} obtained in state-of-the-art PVK solar cells likely produce this condition, and we therefore discuss this aspect in more detail. First, let us recall that V_{OC} and V_{bi} are not fundamentally correlated, i.e., $V_{OC} > V_{bi}$ is a physically possible situation.[34] This is opposite to the traditional relation $V_{OC} < V_{bi}$ applicable to homojunction solar cells, where high built-in voltages are desirable.[35] Homojunction solar cells are provided a built-in voltage solely by doping the p and n regions (Ref. [36], p. 146)) not resorting to work function differences as in the present case. Therefore, minority carrier concentrations and recombination are bound to V_{bi}, whereas in heterojunctions V_{bi} can be changed by modifying the band offsets, without determining the minority carrier concentrations. This additional degree of freedom enables $V_{OC} > V_{bi}$ in heterojunctions.

2.2. Recombination

2.2.1. Bulk Recombination

We develop our models around defect recombination, which imposes the practical limit in solar cells, and extend the results to radiative recombination when necessary. Following Shockley–Read–Hall statistics, the rate of defect recombination depends on the separation ΔE_F of the QFLs, and on the relative position of the defect energy E_t with respect to the QFLs. Thus, if the defect level is located inside the interval between the QFLs E_{Fn} and E_{Fp}, the recombination rate reaches a maximum value given by[5]

$$R_{bulk} = \frac{np - n_i^2}{\tau_{0p}n + \tau_{0n}p} \tag{7}$$

Where n and p are the electron and hole concentrations, τ_{0p} and τ_{0n} are characteristic recombination times for holes and electrons, respectively, and n_i is the intrinsic carrier concentration given by

$$n_i = \sqrt{N_C N_V} e^{-\frac{E_g}{kT}} \tag{8}$$

Here, N_C and N_V are the effective density of states of the conduction and valence band of the absorber layer, respectively, k is Boltzmann's constant and T the absolute temperature. Out of equilibrium, the carrier concentrations n and p are given by

$$n = N_C e^{\frac{E_{Fn} - E_C}{kT}}$$
$$p = N_V e^{\frac{E_V - E_{Fp}}{kT}} \tag{9}$$

with E_C and E_V the electronic energies at the edge of the conduction and valence band, respectively. As a result, the product np contains the QFL splitting according to

$$np = n_i^2 e^{\frac{\Delta E_F}{kT}} \tag{10}$$

Under open-circuit conditions, the total number of photogenerated carriers across the absorber must equal the total number of carriers recombined in the bulk, i.e.

$$Gd = \int_0^d R_{\text{bulk}}(x)\mathrm{d}x \tag{11}$$

where for simplicity we have assumed a homogeneous photogeneration rate G throughout the absorber of thickness d. In the particular case of homogeneous (i.e., independent of x) carrier concentrations within the bulk, this equation simplifies to

$$G = R_{\text{bulk}} \tag{12}$$

This turns to be a good assumption in the ionic solar cell without interface recombination, where under open-circuit the energy bands as well as the QFLs remain horizontal, implying homogeneous concentrations. This is valid when the absorber thickness is much higher than the width of the Debye layers at the interfaces, where the carrier concentrations change appreciably.

While closed-form expressions for R_{bulk} are generally unavailable, we propose different simplifying scenarios that yield analytical solutions, which help us understand the relationship between V_{OC} and energy band offsets. A useful starting point is the limit where we have uniform and equal concentrations, i.e., $n = p$ throughout the absorber. This is also called the "high injection" limit, as it is formally equivalent to the case where photogeneration exceeds any equilibrium carrier concentration. According to Equation (10), the condition $n = p$ implies

$$n = n_i e^{\frac{\Delta E_F}{2kT}} \tag{13}$$

where the QFL splitting must obey $\Delta E_F/q = V_{\text{OC}}$, since ΔE_F does not change with position in this scenario. Assuming identical pseudo-lifetimes for electrons and holes $\tau_{0n} = \tau_{0p} = \tau_0$, the recombination rate from Equation (7) simplifies to

$$R_{\text{bulk}} = \frac{n}{2\tau_0} = \frac{n_i}{2\tau_0} e^{\frac{\Delta E_F}{2kT}} \tag{14}$$

which after applying Equation (12) yields the QFL splitting

$$\Delta E_F|_{\text{min}} = E_g - 2kT \ln\left(\frac{\sqrt{N_C N_V}}{2G\tau_0}\right) \tag{15}$$

Here we use the subscript "min" meaning that this expression corresponds to the lowest possible QFL splitting in the bulk recombination case, for a given photogeneration rate and carrier lifetime.

Now under low injection, depending on the interfacial energies and CTL dopings, the condition $n = p$ is either met only at a single intersection point or entirely avoided, producing higher ΔE_F values.[37] This allows to relate ΔE_F at low injection to $\Delta E_F|_{\text{min}}$ at high injection as follows. If carrier concentrations intersect, the SRH recombination rate adopts a peak-like profile with its peak value R_{bulk}^* given by Equation (14). Thus, we write the integral of $\int_0^d R_{\text{bulk}}(x)\mathrm{d}x = \alpha d R_{\text{bulk}}^*$, where the shape factor

$0 < \alpha \leq 1$ relates the actual area to the rectangular area dR_{bulk}^* given by the peak value. Thus, solving Equation (11) for the QFL splitting we obtain $\Delta E_F = E_g - 2kT \ln[\alpha\sqrt{N_C N_V}/(2G\tau_0)]$, which results in

$$\Delta E_F|_{\text{bulk}} = \Delta E_F|_{\text{min}} + 2kT \ln(1/\alpha) \tag{16}$$

Therefore, we relate the QFL splitting under low injection to the high injection value $\Delta E_F|_{\text{min}}$, highlighting that the narrower the peak-like recombination profile becomes ($\alpha \to 0$), the higher the required R_{bulk}^*, and the higher results ΔE_F. As an example, **Figure 2** shows two recombination profiles: one where $R_{\text{bulk}}(x)$ is uniform as in high injection, and a triangle-shaped profile where the upper vertex corresponds to R_{bulk}^*. Since under open-circuit both are required to have identical areas, the triangle profile doubles the height of the uniform profile, i.e., implying shape factor $\alpha = \frac{1}{2}$.

2.2.2. Interface Recombination

Considering recombination at one single interface with a rate R_{int}, the total number of photogenerated carriers must equal the total number of carriers recombined at the interface, i.e., Equation (11) turns into

$$Gd = R_{\text{int}} \tag{17}$$

The recombination rate is expressed analogously to Equation (7), and assuming again that the defect level is between the QFLs, as in **Figure 3**, the recombination reaches a maximum rate given by[5]

$$R_{\text{int}} = \frac{n^- p^+ - n_{i,\text{int}}^2}{n^-/S_p + p^+/S_n} \tag{18}$$
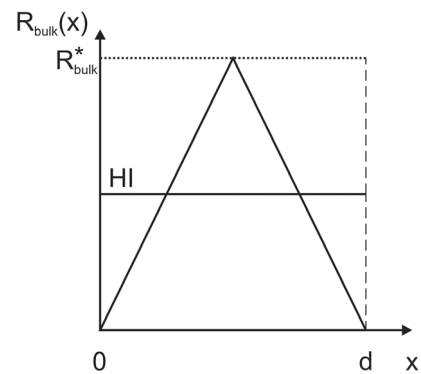

Figure 2. Geometrical appreciation of the shape of the bulk recombination rate profile $R_{\text{bulk}}(x)$ and its impact on open-circuit voltage. The uniform profile (continuous horizontal line) corresponds to the case of high injection conditions, with identical concentrations of electrons and holes throughout the absorber. The triangle profile corresponds to intercrossing carrier concentrations, producing a peak recombination rate R^*_{bulk}. Since at open-circuit the area under both profiles must be the same in order to match photogeneration (cf. Equation (11)), the height of the triangle-shaped profile doubles the height of the uniform profile, resulting a shape factor $\alpha = 1/2$ (see definition in main text).
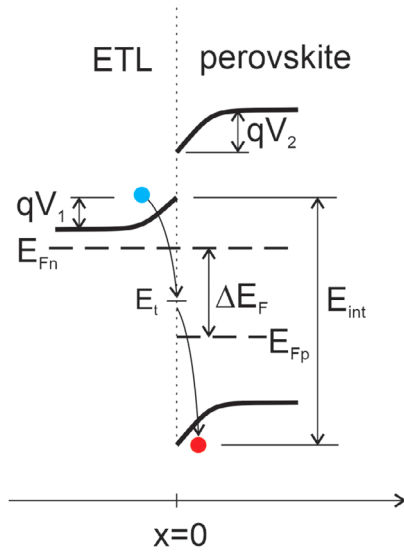
Figure 3. Close-up band diagram denoting the relevant magnitudes at the ETL/perovskite interface for case (c) of Figure 1, showing an electron–hole recombination process through an interface defect level at the energy E_t.

Here, n^- and p^+ are the electron and hole concentrations immediately at the left ($-$) and right ($+$) of the interface under consideration, respectively, while S_p and S_n are the recombination velocities for holes and electrons, respectively. Moreover, with the effective interface bandgap E_{int} defined in Figure 3, the effective intrinsic carrier concentration at the interface can be expressed by[5]

$$n_{i,int} = \sqrt{p_0^+ n_0^-} = \sqrt{N_C^- N_V^+} e^{-\frac{E_{int}}{2kT}} \tag{19}$$

where the subscript '0' denotes thermodynamic equilibrium, N_C^- and N_V^+ are the effective density of states seen at each side of the interface. Since we are interested on the impact of band offsets and band bendings on recombination, we now proceed to describe Equation (18) in terms of interface energies. Figure 3 defines the involved energies in the band diagram of the ETL/absorber interface out of equilibrium, i.e., showing some QFL splitting. At the interface (dotted vertical line) we depicted an electron–hole recombination process occurring through an interface defect at the energy E_t, as well as the band bendings qV_1 and qV_2, and the conduction band offset ΔE_C.

Out of equilibrium, the interface carrier concentrations are given by

$$n^- = N_C^- e^{\frac{E_{Fn} - E_C^-}{kT}}$$
$$p^+ = N_V^+ e^{\frac{E_V^+ - E_{Fp}}{kT}} \tag{20}$$

With E_C^- and E_V^+ the conduction and valence band energies at the left and right of the interface, respectively. With Equation (19), the product $n^- p^+$ is given by

$$n^- p^+ = N_C^- e^{\frac{E_{Fn} - E_C^-}{kT}} N_V^+ e^{\frac{E_V^+ - E_{Fp}}{kT}} = n_{i,int}^2 e^{\frac{\Delta E_F}{kT}} \tag{21}$$

which is the analogue to Equation (10) for interfaces. The exponents in Equation (20) can be written as a function of the

interface energies, as shown next. From Figure 3, notice that $E_{Fn} - E_C^- = qV_1 + q\xi_n$, and $E_V^+ - E_{Fp} = E_{int} - \Delta E_F - (qV_1 + q\xi_n)$, which contains the QFL splitting at the interface. Further, since the conduction band offset is given by

$$\Delta E_C = E_g - E_{int} \tag{22}$$

we rewrite $E_V^+ - E_{Fp} = E_g - \Delta E_C - \Delta E_F - (qV_1 + q\xi_n)$. Therefore, both n^- and p^+ can be seen to be exponentially dependent on both qV_1, ΔE_C, reflecting the interdependence of recombination rate with band bendings and offsets. In the next section we find explicit relations between these quantities.

As a final point, it is important to note that Equation (20) and (21) are only valid under the assumption of non-degenerate carrier concentrations at the interface, i.e., the QFLs are at least an energy $3 kT$ away from the band edges. In the case of strong carrier accumulation at the interfaces, these equations are to be replaced with the corresponding Fermi–Dirac integral expressions (Ref. [38], p. 19) This situation is taken care of by the numerical model, presented below.

3. Modeling

3.1. Numerical Model

We performed simulations of open-circuit voltage and current voltage-characteristics using the widely-spread open source numerical solver IonMonger.[39] This software simulates one-dimensional drift–diffusion transport and electrostatics of free carriers coupled to one mobile and one fixed ionic species in three-layered structures (as in Figure 1). The model is oriented to metalorganic PVKs where ion migration is assisted by vacancies, resulting in anions being the immobile and cations the mobile species.[40,41] The net ionic charge is assumed zero, i.e., the mean concentrations of the positive as well as the negative ions are identical, given by N_0. Recombination is modeled using Shockley–Read–Hall and radiative recombination. Interface recombination is expressed in terms of surface recombination velocities and Shockley–Read–Hall statistics. The simulation parameters are given in Table S1, Supporting Information, assuming values compatible with commonly used ETL materials, a 400 nm-thick PVK with a bandgap of 1.7 eV for the absorber, and, for symmetry, an HTL with identical parameters as the ETL, except for the electron affinity. Since we are interested in cases that potentially lead to high efficiency devices, we assume a good-quality PVK having 30 ns pseudo-lifetimes when bulk defect recombination is activated (leading to carrier diffusion lengths of 550 nm), and low interface recombination velocities of 1000 cm s^{-1} when interface recombination takes place. Bulk radiative recombination is activated in all cases. In the CTLs, carrier concentrations obey Fermi–Dirac statistics, enabling strong carrier accumulation conditions without introducing approximation errors. The majority carrier band offsets are incorporated by setting the electron affinities of the CTLs, according to $\Delta E_C = q(\chi - \chi_{ETL})$ and $\Delta E_V = q(\chi_{HTL} - \chi)$, where χ is the electron affinity of the PVK absorber. Defined in this way, both quantities are positive when the conduction band in the ETL

and the valence band in the HTL favor the separation of photo-generated carriers.

Since we are interested in the device output in steady-state conditions, we record the simulated values of V_{OC} corresponding to the stationary state after light switch-on, starting from thermodynamic equilibrium conditions. In the current-voltage characteristics, we ensure that the time between voltage steps is sufficiently high as to reach steady state at each voltage value before the next voltage step. For the ionic solar cell, this implies that the current–voltage characteristics show no hysteresis, a consequence of the slow voltage scan rate.

3.2. Analytical Expressions at Open-Circuit

Approximate analytical solutions for the QFL splitting (or, equivalently, the implied open-circuit voltage) are available when considering only either bulk or interface recombination. In the following sub-sections, we obtain simple expressions for the QFL splitting ΔE_F in limit cases, distinguishing between pin and ionic solar cell.

3.2.1. Quasi Fermi Level Splitting with Bulk Recombination

a) Case of $\Delta E_C = \Delta E_V > 0$.

This is the case of symmetrical band offsets. In equilibrium, we have crossing carrier concentration profiles: electrons decrease exponentially from the ETL/absorber interface towards the absorber/HTL interface, and holes show a symmetrically opposite profile. Out of equilibrium, the crossing concentration profiles still hold, as identical band offsets do not produce any asymmetry to carrier injection. Depending on the illumination level and bias voltage, the injected carrier concentrations tend to level out the exponentials towards homogeneous (i.e., position independent) profiles in both, the pin and the ionic solar cell. As an example, **Figure 4** shows the concentration profiles obtained from our simulations for both cell types (see next section for simulation details). The carrier concentrations thus flatten out to the

value $n = p = 2\tau_0 G$ predicted by Equation (12) and (14), implying the high injection QFL splitting given by Equation (15). Thus, the solar cell is only able to deliver the minimum possible V_{OC}, for a given recombination lifetime. Although being much closer to each other over the entire absorber than under equilibrium, the carrier concentrations in the pin cell are equal only at the intersection position $x^* = 200$ nm. This results in 12 mV higher open-circuit voltage in the pin cell than in the ionic cell, where both concentrations are identical throughout the absorber (1.175 mV in the pin cell vs 1.166 mV in the ionic cell, cf. Figure 6).

Equation (15) also reflects that under high injection conditions, the impact of defect recombination lifetime on V_{OC} is highest, since the second term implies a 120 mV V_{OC} decrease per order of magnitude in τ_0 decrease, at room temperature, against 60 mV under low injection (cf. cases (b) and (c) below).

b) Case of $\Delta E_C > \Delta E_V > 0$.

Increasing ΔE_C above ΔE_V, implies a decrease in built-in voltage compared to the previous case, and as a result we expect, in principle, a decrease in V_{OC} due to the additional energy loss. However, the differentiation of carrier concentrations introduced by the asymmetry in band offsets can result in higher V_{OC}, as shown below. Further, with sufficiently high offset and lifetime, this scenario opens up the possibility for $V_{OC} > V_{bi}$.

In the pin cell, the condition $V_{OC} > V_{bi}$ reverses the electric field in the absorber, depleting electrons away from the ETL/absorber interface towards the opposite interface, and attracting holes. **Figure 5**a shows the carrier concentrations and the recombination rate profile obtained from our simulations. The resulting intercrossing carrier concentration profiles again bring us to the reasoning about Equation (16), enabling a qualitative explanation for the higher V_{OC} compared to the symmetric case is possible. With the asymmetry introduced by $\Delta E_C > \Delta E_V > 0$, the coordinate x^* where $n = p$ is displaced out of the absorber center, effectively cropping one end of the peak profile of $R_{bulk}(x)$. However, since the area under $R_{bulk}(x)$ must stay constant (Equation (11)), the peak value of R_{bulk} must increase, implying $\alpha < 1$, obtaining higher V_{OC}. Notice that if the asymmetry is
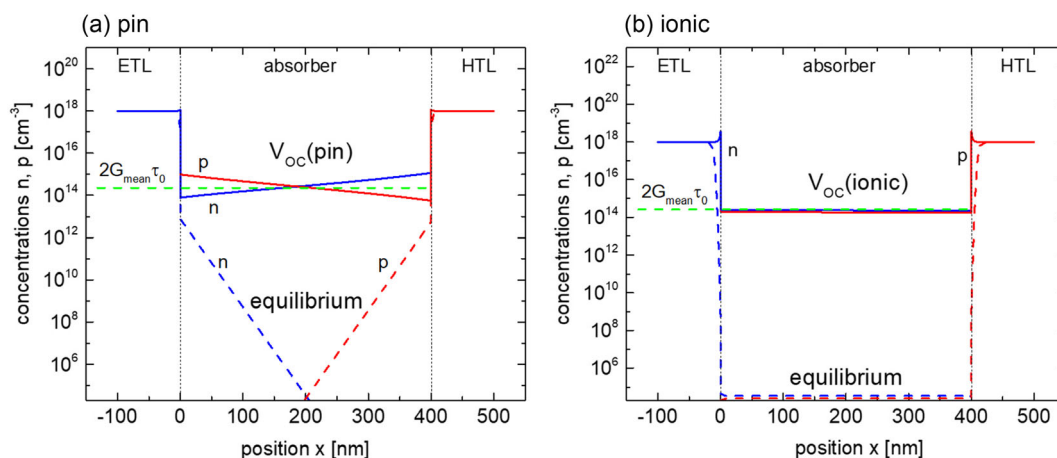
Figure 4. Electron (blue) and hole (red) concentrations at equilibrium (dashed) and open-circuit conditions a) in a pin cell and b) an ionic solar cell, where the absorber is placed between an electron transport layer (ETL) and a hole transport layer (HTL). The interface band offsets are assumed equal at $\Delta E_C = \Delta E_V = 0.2$ eV, producing symmetrical concentration profiles. In the ionic cell, the carrier concentrations are identical throughout the absorber, agreeing with the analytical concentration value (green dashed line) obtained with the mean value of the photogeneration rate G_{mean}.
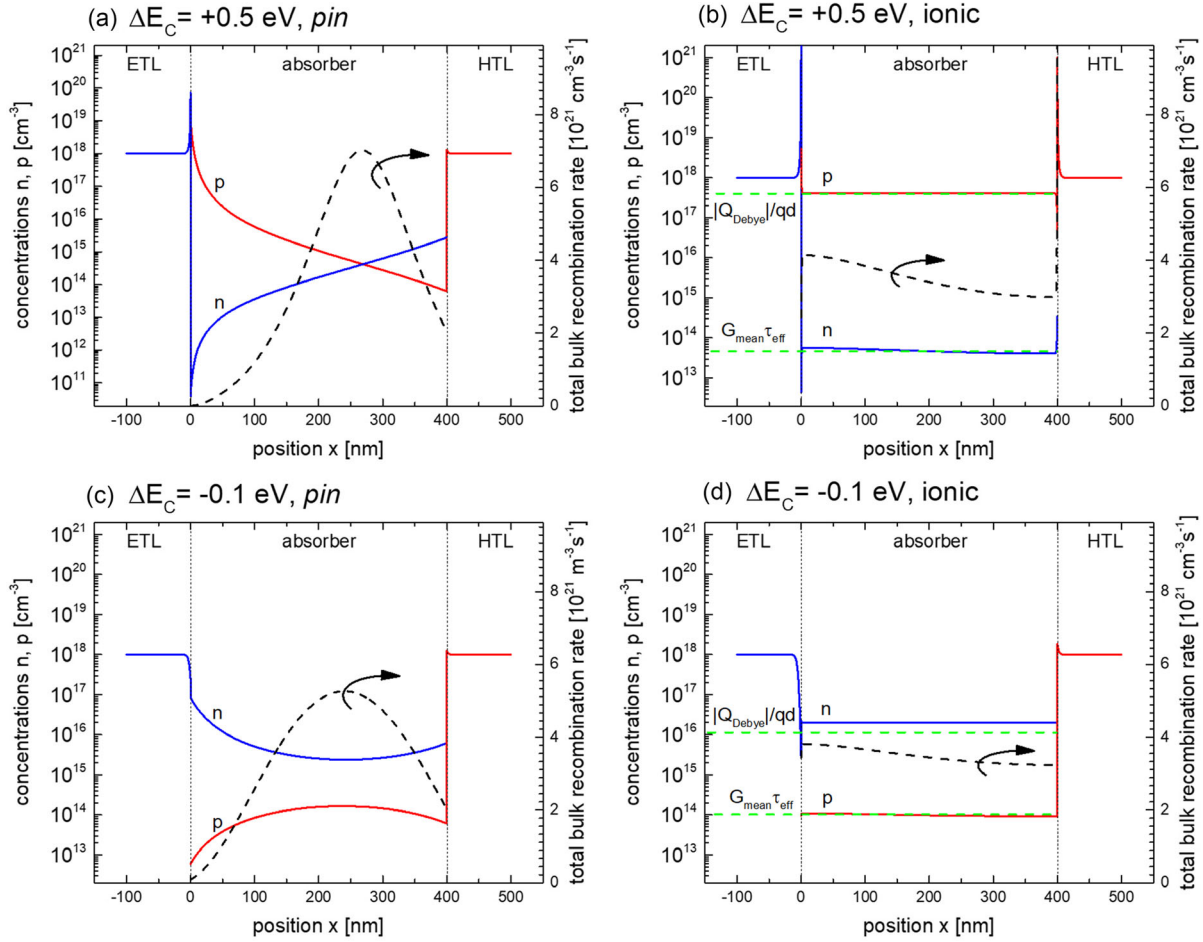
Figure 5. Electron (blue) and hole (red) concentrations (left axes) at open-circuit conditions in the pin cell and in the ionic solar cell with only bulk recombination (right axes, total recombination rate), under two different band offset cases: a) $\Delta E_C = -0.1$ eV and b) $\Delta E_C = 0.5$ eV. The dashed horizontal green lines indicate the values of n and p assumed by the analytical models for each case (see main text).

introduced at the opposite interface, i.e., with $\Delta E_V > \Delta E_C > 0$, this analysis is analogous.

In the ionic solar cell, the band bendings are strongly reduced by V_{OC}, turning negative if $V_{OC} > V_{bi}$. For simplicity, we take the case of a PVK absorber, which after Equation (5) obeys

$$V_{bi} - \Delta E_F|_{bulk}/q = V_1 + V_4 \tag{23}$$

implying negative $V_{1,4} < 0$. Since now the offset at the HTL is the smaller of both offsets, the negative band bendings produces hole accumulation at the HTL interface, resulting in an increased hole concentration within the absorber. In the limit $p \gg n$, Equation (7) is simplified to $R_{bulk} = n/\tau_0$, and with $G = R_{bulk}$ we have $n = G\tau_0$. Solving Equation (10) for n we have

$$R_{bulk} = \frac{n_i^2}{\tau_0 p} e^{\frac{\Delta E_F}{kT}} \tag{24}$$

and the QFL splitting results in

$$\Delta E_F|_{bulk} = E_g - kT \ln\left(\frac{N_C N_V}{\tau_0 G p}\right) \tag{25}$$

Notice that since $p \gg n$ in the whole absorber, the obtained $\Delta E_F|_{bulk}$ limit is valid also for the case of non-negligible radiative recombination when replacing τ_0 with the effective lifetime $\tau_{eff} = (\tau_0^{-1} + \tau_{rad}^{-1})^{-1}$, where the radiative lifetime is given by $\tau_{rad} = (B_{rad} p)^{-1}$, B_{rad} being the radiative recombination constant. An analogous replacement is also valid for the equations obtained when $n \gg p$, as in the next case (c).

The concentration p in Equation (25) is available when considering charge neutrality in the bulk which in our case with $p \gg n$ is expressed by the neutrality condition $q(p + P_{bulk} - N_0) = 0$. With P_{bulk} given by Equation (4) we arrive at

$$p = \frac{Q_{Debye}}{qd} \tag{26}$$

i.e., the hole carrier concentration allowed to flood the absorber from the HTL is tied to the ionic charge at the interface, which is a consequence of assuming a field-free bulk interior. This is

possible under our assumption that the ionic charges dominate the electrostatics even under the increase in free charge carrier concentrations upon illumination and bias voltage. With Equation (25) and (23), we can write

$$V_{bi} - E_g + kT \ln\left(\frac{N_C N_V}{\tau_0 G Q_{Debye}/qd}\right) = V_1(Q_{Debye}) + V_4(Q_{Debye}) \tag{27}$$

where the interface potentials are expressed as a function of the surface charge Q_{Debye}. Following the surface polarization model from Courtier et al.,[30] the interface potentials are given by analytical functions (see Supporting Information), and therefore Equation (27) is solved for Q_{Debye} by root-finding. This yields the concentration p from Equation (26), enabling to calculate the saturation value of $\Delta E_F|_{bulk}$ with Equation (25). Example concentration profiles in Figure 5b shows the agreement between our simulations and the values for p postulated by Equation (26).[42]

c) Case of $\Delta E_C < \Delta E_V$ with $\Delta E_V > 0$.

The lower offset at the ETL interface produces accumulation of electrons at the absorber side of the ETL/absorber interface ($x = 0$), and depletion at the ETL side. For sufficiently low ΔE_C, the strong electron accumulation at the interface produces in $n \gg p$ throughout the absorber also under illumination, as shown by the simulated concentration profiles shown in Figure 5c,d. This implies that high injection conditions are avoided throughout the absorber, which results in a higher QFL splitting than in the case of symmetrical offsets.

In the pin solar cell, an analytical solution to find the QFL splitting is not available; we find however good agreement with the simulations when assuming $\alpha = 1/3$ in Equation (16) to obtain the saturation value of ΔE_F, as shown in the next section.

In the ionic solar cell, the condition $n \gg p$ leads to an analogous analysis to case (b) above, now requiring $n = Q_{Debye}/qd$,[43] which again leads to Equation (27) when assuming a PVK absorber. The resulting ΔE_F is different to case (b) due to the higher V_{bi}, resulting in a lower limit value than with the smaller built-in voltage case of $\Delta E_C > \Delta E_V > 0$ given above.

3.2.2. Quasi Fermi Level Splitting with Interface Recombination

At each interface, we have the local quasi-Fermi level splittings $\Delta E_F|_{ETL}$ and $\Delta E_F|_{HTL}$, where the ETL and HTL denote each of the interfaces. Since the interface with higher recombination ultimately determines the lower QFL splitting, we separately find expressions for $\Delta E_F|_{ETL}$ and $\Delta E_F|_{HTL}$ assuming that recombination takes place at one interface. Since no bulk recombination is considered here, we bear in mind that the relations obtained below are ultimately limited by the bulk recombination limits found in the previous sub-section. Further, we consider the offset ΔE_C as variable, and fix ΔE_V; the opposite case is derived by analogy to the equations obtained here.

a) Recombination at the ETL/absorber interface.

Assuming low injection conditions at the interface, we have $n^- \gg p^+$ (see ref. [5], p. 7] for a derivation under high injection conditions). For simplicity, we further assume equal recombination velocities for electrons and holes, defining $S_E = S_n = S_p$, and

neglect $n_{i,int}^2$ in Equation (18), which replacing in Equation (17) results in $Gd = S_E p^+$, i.e.,

$$Gd = S_E \frac{n_{i,int}^2}{n^-} e^{\frac{\Delta E_F}{kT}} \tag{28}$$

In the ETL, the electron concentration away from the interface corresponds to the doping concentration, i.e., $n = N_D$. At the interface, the concentration n^- is obtained as a function of N_D and the band bending qV_1 according to

$$n^- = N_D e^{-qV_1/kT} = N_{CE} e^{-q(V_1 + \xi_n)/kT} \tag{29}$$

where $N_C^- = N_{CE}$ is the conduction band density of states in the ETL. Replaced in Equation (28) together with Equation (19) and (22), this yields the QFL splitting

$$\Delta E_F|_{ETL} = E_g - qV_1 - q\xi_n - \Delta E_C - kT \ln\left(\frac{S_E N_V}{Gd}\right) \tag{30}$$

In order to better understand this and the forthcoming equations, it is convenient to recall that the energies are related to enthalpies, while the last term containing recombination physics, corresponds to entropic losses.[33] Thus, for example, the appearance of the absorber thickness d in the entropic term reflects that the impact of interface recombination dilutes with increasing absorber volume. Moreover, when assuming the condition $\Delta E_C \geq 0$, desirable for undisturbed photocurrent extraction, Equation (30) exposes the enthalpic loss introduced by positive ΔE_C, with a linear decrease of ΔE_F with ΔE_C. In the opposite direction, decreasing ΔE_C, we have an increase of ΔE_F up to a saturation value that depends on interface electrostatics: without ions (pin solar cell), when ΔE_C reaches sufficiently negative values we have electron accumulation, and we approach $qV_1 \rightarrow -\Delta E_C$. Replaced in Equation (30), this produces the saturation value

$$\Delta E_F|_{ETL} = E_g - q\xi_n - kT \ln\left(\frac{S_E N_V}{Gd}\right) \tag{31}$$

In the ionic solar cell we have $qV_1 > -\Delta E_C$, and Equation (30) predicts a smaller ΔE_F limit, as shown by our simulations in next section.

b) Recombination at the absorber/HTL interface.

Analogously to case (a) above, and assuming $S_H = S_n = S_p$, we solve for $\Delta E_F|_{HTL}$ taking into account that at this interface the concentrations obey $p^+ \gg n^-$, Equation (17) simplifies to $Gd = S_H n^-$, and we obtain

$$Gd = S_H \frac{n_{i,int}^2}{p^+} e^{\frac{\Delta E_F}{kT}} \tag{32}$$

The hole concentration p^+ at the HTL side of the interface is given by

$$p^+ = N_A e^{-qV_4/kT} = N_H e^{-q(V_4 + \xi_p)/kT} \tag{33}$$

where N_A is the acceptor dopant concentration, and $N_H = N_V^+$ is the valence band density of states in the HTL. Replacing in Equation (32), the QFL splitting becomes

$$\Delta E_F|_{HTL} = E_g - qV_4 - q\xi_p - \Delta E_V - kT \ln\left(\frac{S_H N_C}{Gd}\right) \quad (34)$$

The impact of the band offset ΔE_V on ΔE_F is deduced and interpreted analogously to case (a) above. Here, we are interested in finding a relation between ΔE_F and ΔE_C, at a fixed ΔE_V. This is possible when relating qV_4 to the offset ΔE_C, as shown below.

In the pin solar cell, the band bending qV_4 is negligible when $\Delta E_C \leq \Delta E_V$, and Equation (34) yields the QFL splitting independent of ΔE_C. When $\Delta E_C > \Delta E_V$, however, a non-negligible band bending $qV_4 < 0$ appears at the interface, resulting in an increasing ΔE_F with ΔE_C, which saturates to the limit imposed by bulk recombination.

In the ionic solar cell, the band bending qV_4 leads to a monotonous increase of ΔE_F with ΔE_C, as shown next. We resort to Equation (23), which, evaluated with $V_1 = V_4$ (see next section), delivers

$$qV_4 = \frac{1}{2}\left(E_g - \Delta E_C - \Delta E_V - q\xi_n - q\xi_p - \Delta E_F\right) \quad (35)$$

Replacing this expression into Equation (34) and solving for the QFL splitting, we arrive at

$$\Delta E_F|_{HTL} = E_g - \Delta E_V + \Delta E_C + q\xi_n - q\xi_p - 2kT \ln\left(\frac{S_H N_C}{Gd}\right) \quad (36)$$

which shows a monotonous increase of ΔE_F with ΔE_C, i.e., with decreasing built-in voltage. This is understood when considering p^+ in Equation (32) as follows: with sufficiently large offset ΔE_C we eventually reach the condition $V_{OC} > V_{bi}$, which implies negative V_4, producing the accumulation of holes at the HTL side of the interface. This results in p^+ increasing with ΔE_C, which implies a concomitant increase of ΔE_F for Equation (32) to hold.

From the technological point of view, this case is of special interest, because it enables to reduce interface recombination at one interface by increasing the band offset at the opposite interface. In the next section we show that the resulting increase in V_{OC} goes hand-in-hand with an increase in efficiency.

4. Results

4.1. Open-Circuit Conditions

Figure 6 shows the results for bulk recombination only, with the simulated open circuit voltage V_{OC} (symbols) and calculated QFL splitting ΔE_F (dashed lines) as a function of the conduction band offset ΔE_C at the ETL/absorber interface. For reference, the radiative absolute limit corresponding to the chosen absorber bandgap of $E_g = 1.7$ eV is shown by the orange dashed line at $V_{OC} = 1.4$ V, valid for unconcentrated AM1.5 G spectrum radiation.[44] We compare simulation results for the ionic solar cell (filled symbols), containing a high mobile ion concentration $N_0 = 10^{20}$ cm^{-3}, and the ion-free, pin solar cell (open symbols). The top axis in Figure 6 shows the built-in voltage, calculated as $V_{bi} = 1.3V - \Delta E_C/q$ resulting from Equation (2) and the chosen CTL doping levels (values given in Table S1, Supporting Information). As seen in Figure 6, the overall trends observed
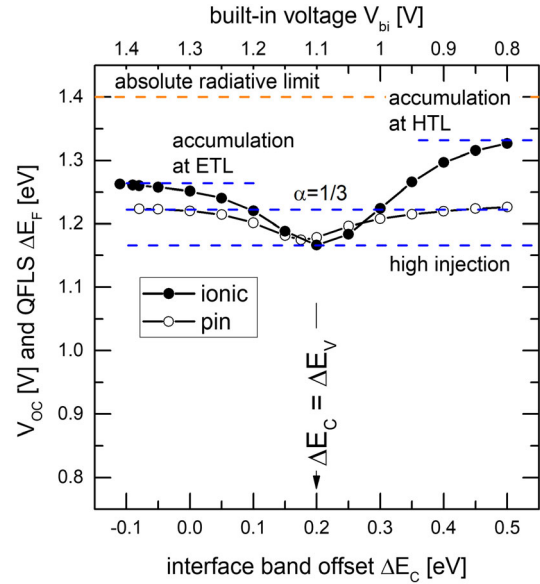
Figure 6. Simulated open-circuit voltage V_{OC} (symbols) and modeled quasi-Fermi level splitting ΔE_F (dashed lines) as a function of the conduction band offset ΔE_C at the ETL/absorber interface. Open symbols correspond to V_{OC} in the ion-free case, full symbols assume positive as well as negative ion concentrations of $N_0 = 10^{20}$ cm^{-3}, the positive ions being mobile. The blue horizontals predicted by the equations for the different limit cases, as indicated. With the assumed parameters, the worst-case condition is $\Delta E_C = \Delta E_V$, which at open-circuit produces high injection conditions in all the extension of the absorber. The orange horizontal line shows the radiative limit of 1.4 V corresponding to a gap of $E_g = 1.7$ eV.

for the ionic and the pin cell are similar. For instance, the minimum open-circuit voltage and QFL splitting is nearly the same for both devices, occurring at $\Delta E_C = \Delta E_V$, corresponding to the high injection limit from Equation (15), shown by the dashed horizontal in Figure 6. When choosing higher or lower ΔE_V values, the minimum follows this condition (not shown here). In the asymmetric case where band offsets are unequal, the carrier concentrations move away from high injection conditions, resulting in higher V_{OC} for both devices. At the chosen limits for ΔE_C, V_{OC} saturates to different values depending on the presence of mobile ions. In the limit at $\Delta E_C = 0.5$ eV, V_{OC} in the ionic solar cell surpasses the pin solar cell by 100 mV, with the saturation value agreeing with ΔE_F from Equation (25), where p is calculated by Equation (26) and (27). In the opposite limit at $\Delta E_C = -0.1$ eV, the ionic solar cell saturates at a 40 mV higher V_{OC} than the pin cell, also agreeing with the saturation value obtained as in the previous case.

The pin solar cell, in contrast, saturates at both extremes to the value predicted by Equation (16) when assuming a shape factor $\alpha = 1/3$, although with different concentration profiles, shown in Figure 5a,c: when $\Delta E_C > \Delta E_V$, the crossing profiles imply $p(x^*) = n(x^*)$, while when $\Delta E_C > \Delta E_V$, we have $p(x) < n(x)$.

Figure 7 shows the band bendings qV_1 (circles) and qV_4 (crosses) obtained from the simulations in equilibrium (black symbols) and under open-circuit conditions (pink, orange) for the pin (plot a) and the ionic solar cell (plot b). The band bendings qV_2 and qV_3 are not shown because they are negligible due to the higher dielectric constant assumed in the absorber layer than in the CTLs, mimicking
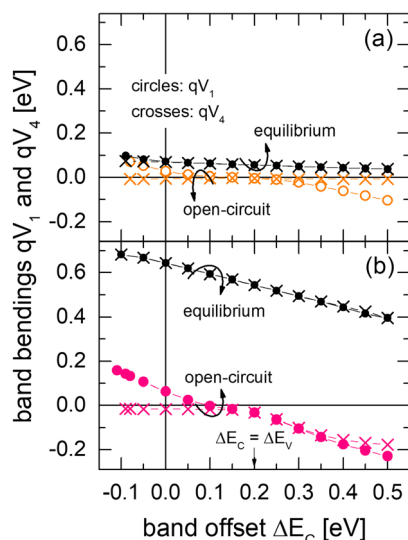
Figure 7. Band bendings at the side of the charge-transport layers (qV_1: ETL, qV_4: HTL) occurring in equilibrium (black symbols) and under illumination, in open-circuit conditions (colored symbols) in the pin (plot a) and the ionic solar cell (plot b), as a function of the band offset ΔE_C at the ETL/absorber interface.

Figure 8. Open-circuit voltage V_{OC} (simulations, symbols) and quasi-Fermi level splitting ΔE_F (analytical model, lines) as a function of the conduction band offset ΔE_C. Open symbols correspond to V_{OC} in the pin cell (ion-free case), full symbols correspond to the ionic cell, where we assume positive as well as negative ion concentrations of $N_0 = 10^{20}\,\text{cm}^{-3}$. The simulations assume interface recombination either at the ETL/absorber (blue), absorber/HTL (red) or both interfaces (green), with only radiative recombination in the bulk. The different approximations from the analytical model are explained in the main text. The saturation of V_{OC} at the extremes of the band offset occurs due to pinning (blue, $\Delta E_C = -0.1\,\text{eV}$), or bulk radiative recombination (red, $\Delta E_C = 0.5\,\text{eV}$).

the case of metal-halide PVK solar cells (values given in Table S1, Supporting Information). The behavior of the band bendings for the pin solar cell is explained in the Supporting Information, see Figure S1 and corresponding paragraph.

The ionic solar cell, Figure 7b, shows much larger equilibrium band bendings than the pin solar cell due to the large assumed ion concentrations, which are able to accommodate the built-in voltage at both interface Debye layers (e.g., at $\Delta E_C = 0$ in equilibrium we have $V_1 + V_4 = 1.28\,\text{V}$, almost equal to the built-in voltage $V_{bi} = 1.3\,\text{V}$). Under open-circuit voltage conditions, both band bendings decrease to hold Equation (5), however with different proportions, depending on the relation between ΔE_C and ΔE_V. Following Equation (5), both band bendings turn negative as soon as $V_{OC} > V_{bi}$, which in our case occurs at around $\Delta E_C = 0.1\,\text{eV}$, corresponding to $V_{bi} = V_{OC} = 1.2\,\text{V}$ (cf. Figure 6, open circles). This crossover band offset value therefore depends on recombination parameters and built-in voltage.[45] Moreover, notice that below $\Delta E_C = 0.1\,\text{eV}$, qV_4 remains close to zero but negative, and independent of the band offset. This is related to the fact as discussed in Section 3.2.1, since $\Delta E_C < \Delta E_V$ in this regime.

The case of interface recombination is shown in **Figure 8**, displaying the results for simulated V_{OC} (symbols) and modeled QFL splitting ΔE_F (dotted lines), as a function of the conduction band offset ΔE_C at the ETL/absorber interface. Here, the only bulk recombination mechanism is radiative, imposing the absolute limit shown by the dashed orange horizontal. Results for the ionic solar cell are shown with filled symbols (mobile ion concentration $N_0 = 10^{20}\,\text{cm}^{-3}$), while results for the ion-free, pin solar cell, are shown with open symbols. The case of recombination at the ETL/absorber interface is shown in blue (symbols and lines), at the absorber/HTL interface by green, and red when corresponds with recombination at both interfaces, assuming identical recombination velocities.
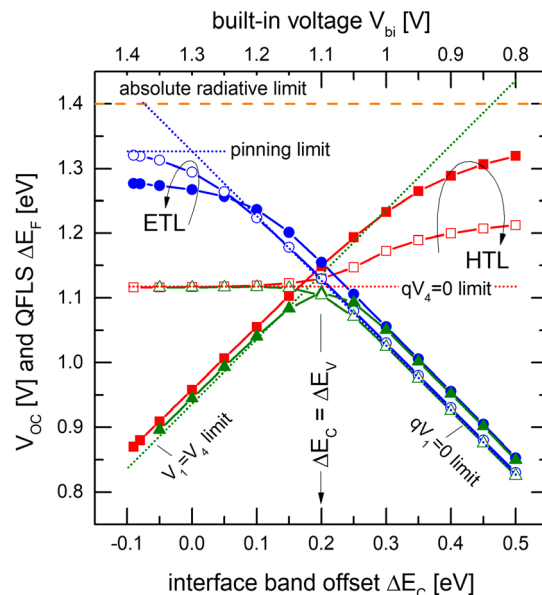
Depending on the recombination active interface, and the presence of ions, the results from Figure 8 show very distinctive trends for the open-circuit voltage: 1) With recombination at the ETL/PVK interface only (blue symbols), V_{OC} decreases with ΔE_C, and therefore with decreasing V_{bi}. This case reflects the most intuitive case of ΔE_C directly implying an energy loss of carriers. The saturation towards $\Delta E_C < 0$ occurs in both solar cells, with the pin solar cell saturating at higher values. At $\Delta E_C = -0.1\,\text{eV}$, the simulations show that V_{OC} becomes in part limited by bulk radiative recombination: integrating the recombination profiles across the absorber, we obtained a radiative recombination current of $11.5\,\text{mA}\,\text{cm}^{-2}$ and an interface recombination current of $10.8\,\text{mA}\,\text{cm}^{-2}$ (for a total of $22.3\,\text{mA}\,\text{cm}^{-2}$, equating the photogeneration current). The blue dotted lines in Figure 8 correspond to the model predictions for negligible qV_1 and pinning cases from Equation (30) and (31), respectively. The band bendings obtained in the simulations are shown below. 2) In the case of recombination at the PVK/HTL interface only (red symbols in Figure 8), the pin solar cell (open red squares) shows V_{OC} independent of ΔE_C up to the condition $\Delta E_C = \Delta E_V$, with the corresponding value of ΔE_F given by Equation (34) with $qV_4 = 0$. When $\Delta E_C > \Delta E_V$, V_{OC} increases towards saturation by bulk radiative recombination, to practically the same saturation value as in the bulk recombination case (cf. Figure 6). The ionic solar cell (filled red squares), on the contrary, shows a steady increase of V_{OC} with ΔE_C, which is governed by the condition of equal

band bendings $qV_1 = qV_4$, given by Equation (36) (red dotted line in Figure 8). At high ΔE_C, the ionic solar cell saturates at higher V_{OC} values than the pin cell, due to interface recombination becoming weakened as ΔE_C increases (cf. Equation (36)), being bulk radiative recombination the limiting mechanism. The saturation value is 10 mV lower value than with bulk recombination only (cf. Figure 6) because interface recombination is non-negligible at $\Delta E_C = 0.5$ eV. At this extreme, the simulations indicate that interface and bulk radiative recombination have nearly equal shares on total recombination. Thus, increasing the band offset at the opposite interface (here the ETL/absorber interface) where interface recombination occurs (here the absorber/HTL interface), effectively reduces the impact of interface recombination. Therefore, this can be seen as an indirect strategy to mitigate recombination at one specific interface. 3) The case of identical recombination velocities at both interfaces (green symbols), is directly understood as a superposition of both previous cases. With $\Delta E_C < \Delta E_V$, in the pin as well as the ionic solar cell, we see that V_{OC} is limited by the recombination at the PVK/HTL interface, while with $\Delta E_C > \Delta E_V$, recombination at the ETL/PVK interface governs V_{OC}. In the more general case of non-identical interface recombination velocities, the simulations show the maximum V_{OC} shifting towards $\Delta E_C < \Delta E_V$ when $S_{ETL} > S_{HTL}$, and towards $\Delta E_C > \Delta E_V$ when $S_{ETL} < S_{HTL}$ (see Figure S2, Supporting Information).

In order to verify the validity of the different band bendings assumed in the analytical models, **Figure 9**a–c shows the band bendings qV_1 and qV_4 obtained from the simulations of the ionic solar cell (see Figure S3, Supporting Information, for the pin cell). For reference, the equilibrium values of qV_1 and qV_4 are shown with black symbols. Starting with the case of ETL/absorber recombination, Figure 9a shows that at V_{OC} (blue symbols) the band bendings turn negligible at an offset value of ≈ 0.1 eV. This value is deduced by the condition $V_{bi} = V_{OC}$, as commented for the bulk recombination case. The negligible band bendings result in the linear decrease of V_{OC} seen in Figure 8 above $\Delta E_C = 0.2$ eV. With ΔE_C decreasing towards negative values, qV_4 remains negligible, while qV_1 increases due to the accumulation of electrons at the ETL/absorber interface, eventually reaching electron Fermi level pinning (see case (a) in Section 3.2.2).

Turning to the case of interface recombination at the absorber/HTL interface in the ionic solar cell (Figure 9b), the simulations show nearly identical band bendings over the largest part of the studied range, validating the assumption $qV_1 = qV_4$ from the model.

In the special case where both interfaces have identical recombination velocities, we obtain the red symbols in Figure 9c. Here, when $\Delta E_C < \Delta E_V$, the band bendings follow the trend from recombination at the absorber/HTL interface (cf. Figure 9b), while with $\Delta E_C > \Delta E_V$ we have the behavior from the ETL/absorber interface (cf. Figure 9a).

4.2. Solar Cell Output

The dependence of all electrical solar cell output parameters obtained from simulated current/voltage characteristics is now analyzed as a function of the conduction band offset ΔE_C,
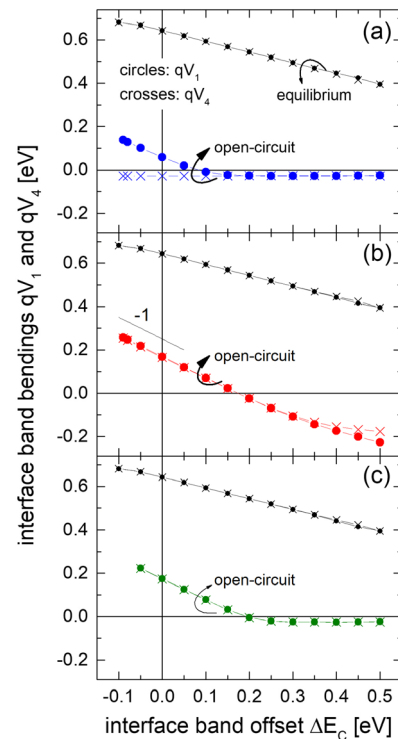

Figure 9. Simulation results for the ionic solar cell with interface defect recombination. Decrease of interface energy band bendings qV_1 and qV_4 with the band offset ΔE_C at the ETL/absorber interface in thermodynamic equilibrium (black) and under illumination, open circuit conditions (colored symbols), for three recombination locations: a) ETL/absorber interface (blue), b) absorber/HTL interface (red), c) both interfaces (green). The straight line in (b) shows the slope-1 for reference.

keeping $\Delta E_V = 0.2$ eV (analogous results correspond to the opposite case of varying ΔE_V at a fixed ΔE_C). **Figure 10** shows the open-circuit voltage V_{OC}, short-circuit current density J_{SC}, fill factor FF, and photoconversion efficiency (PCE), as a function of ΔE_C. Plot column (a) shows the output parameters with bulk recombination only, column (b) for ETL/absorber interface recombination, and column (c) for absorber/HTL interface recombination. Filled symbols correspond to the ionic solar cell, and open symbols to the pin solar cell.

Comparing the PCE in pin and ionic solar cells, the results with ΔE_C obtained for the three cases are markedly dissimilar, including regions where the trends are in opposite directions. Comparing the results for PCE and V_{OC} in Figure 10a–c we notice that this originates in the V_{OC} vs. ΔE_C dependence, plus the higher J_{SC} from the pin cell. The higher short-circuit current originates in the enhanced photocarrier collection provided by the internal electric field in the pin cell, which is absent in the ionic solar cell.

In the region $\Delta E_C < \Delta E_V$ (left of the dashed vertical lines in Figure 10), regardless of the location of recombination (bulk or interfaces), the pin solar cell clearly surpasses the PCE of the ionic solar cell. In the region $\Delta E_C > \Delta E_V$, however, the ionic solar cell delivers increasingly higher efficiency than the pin cell when only bulk defect recombination (column a) or recombination at the absorber/HTL interface (column c) dominate. In the
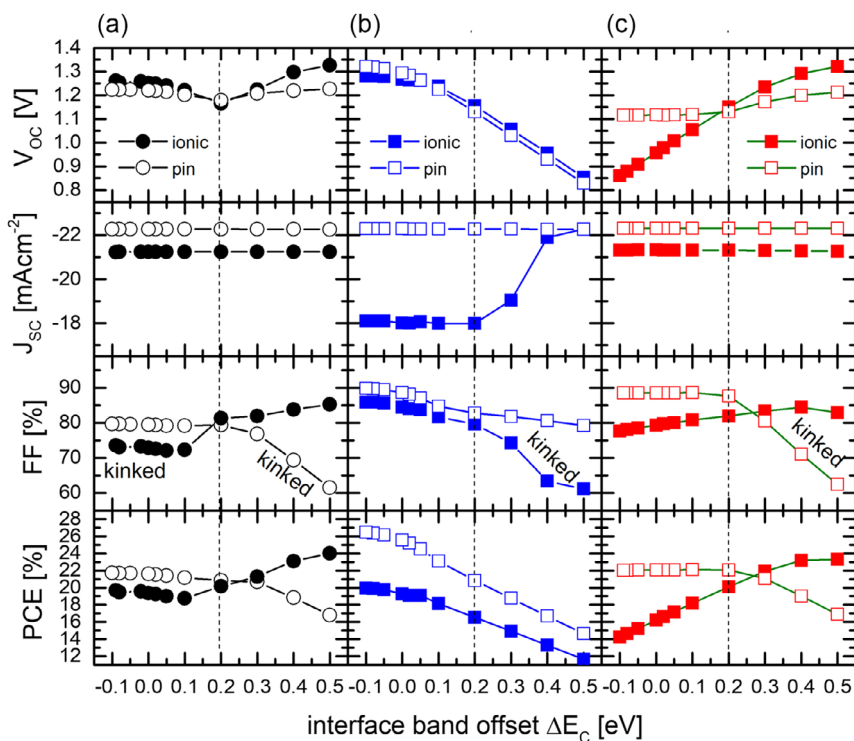
Figure 10. Solar output parameters as a function of the ETL/absorber interfacial energy offset ΔE_C, simulated for the case of bulk defect recombination (plot column a), ETL/absorber interface recombination (column b), and absorber/HTL interface recombination (column c). Overall, we notice the highly distinctive ΔE_C dependence of photoconversion efficiency (PCE) among the three cases. See main text for discussion.

latter case, at the saturation offset of $\Delta E_C = 0.5$ eV, the ionic solar cell reaches 23% efficiency, well above the pin solar cell at PCE = 17%. Both declines in PCE of the pin cell are explained by a sharp loss in fill factor with increasing ΔE_C, which originates in the loss of photocurrent, marked by a kink (labeled in Figure 10) in the current/voltage characteristics (see below). The photocurrent loss is caused by the reversal of electric field at maximum power point voltage V_{mpp} in the pin cell, which opposes carrier collection. The electric field reverses when $V_{mpp} > V_{bi}$, a condition which becomes increasingly possible when reducing V_{bi} with the increase of ΔE_C. This is seen in the current/voltage characteristics shown in **Figure 11**, which correspond to the extreme offset values $\Delta E_C = -0.1$ and $+0.5$ eV, and to the symmetrical case of $\Delta E_C = \Delta E_V = 0.2$ eV leading to high injection conditions. The case of $\Delta E_C = 0.5$ eV, $\Delta E_C > \Delta E_V$, is represented in the last row of graphs in Figure 11, where the $J(V)$ curves of the pin cell (dashed lines) show a kink in both bulk and absorber/HTL recombination. The kink starts at 0.8 V bias, which matches $V_{bi} = 0.8$ V (corresponding to $\Delta E_C = 0.5$ eV), marking the reversal in the electric field. The reversed electric field opposes the collection of photogenerated carriers, producing a loss in photocurrent with increasing voltage, and therefore the drop in FF shown in Figure 10a,c. In the ionic solar cell, this is avoided because the ions shield the field in the absorber, not allowing any opposing field. As an example, Figure S4, Supporting Information, compares the band diagrams of both cells at 1 V bias voltage for the case of bulk recombination, showing the reversed electric field occurring in the pin cell.

Turning to the case of interface recombination at the ETL/absorber only (column b in Figure 10), the PCE of both cells decreases with the band offset, with the pin cell always surpassing the ionic cell by $\approx 25\%$ relative. This is accounted for by the strong loss in fill factor in the ionic solar cell, also producing kinked characteristics, as shown in Figure 11b at $\Delta E_C = 0.5$ eV.

From the technological point of view, our results reveal that the presence or absence of ions implies strikingly different solar performance optimization paths. If the band offset at the interface with dominating recombination is adjustable (e.g., by surface treatments), it should be minimized to minimize carrier energy losses and maximize V_{OC}. In our simulations, this is the case of ETL/absorber recombination, where we varied ΔE_C. If the band offset at the interface with dominating recombination is fixed (here the case of HTL surface dominating interface recombination) we require to increase the band offset at the opposite interface in order to maximize V_{OC}, despite the concomitant drop in built-in voltage. This originates in the possibility to produce majority and minority carrier concentrations in the nominally intrinsic absorber when mobile ions control the absorber´s electrostatics, as discussed above. This might be the case of a recent experimental study involving inorganic $CsPbI_{1.8}Br_{1.2}$ PVK solar cells.[22] Using an ETL material with a high offset of $\Delta E_C = 0.4$ eV, compared to the baseline ETL having $\Delta E_C = 0.25$ eV, the authors obtained not only higher photocurrent due to the increased charge separation,[22] also a 100 mV higher open-circuit voltage, which is compatible with our results from Figure 10. This comparison is subject to the occurrence of a
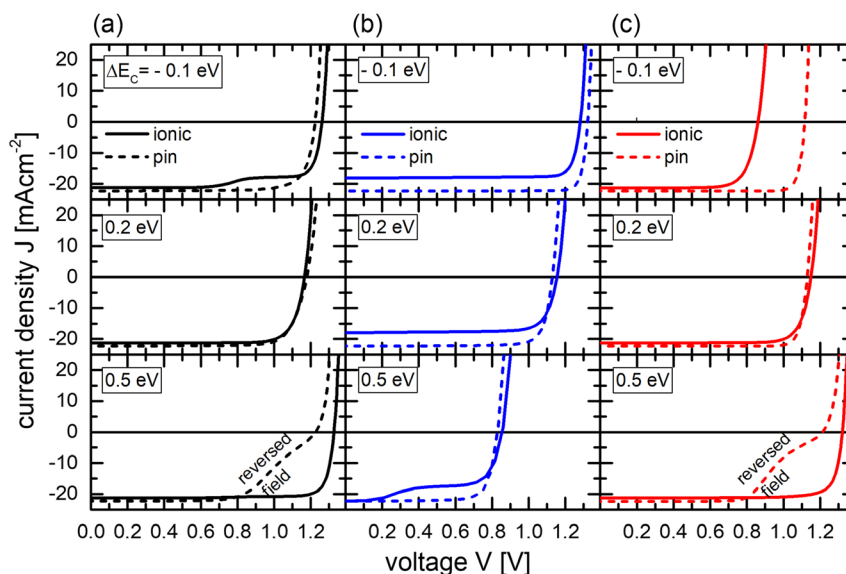
Figure 11. a) Current/voltage characteristics corresponding to pin (dashed) and ionic (solid) cells with only bulk, b,c) ETL/absorber or absorber/HTL recombination, having ETL/absorber conduction band offsets ΔE_C of -0.1, 0.2, and 0.5 eV. The valence band offset at the absorber/HTL interface is fixed at $\Delta E_V = 0.2$ eV. With $\Delta E_C = 0.5$ eV, the resulting $V_{bi} = 0.8$ V implies that the pin solar cell suffers from reversed electric field when $V > 0.8$ V, severely reducing the photocurrent and the fill factor of the $J(V)$ characteristics.

very high density of mobile ion concentration being present in the cells reported in ref. [22], which is possible in the chosen PVK material.[46]

4.3. Notes on the Adopted Methodology and Model

Let us remark that the high doping levels and mobilities chosen for the CTLs rendered negligible losses in these layers. Nevertheless, Figure S5, Supporting Information, shows further simulations with up to two orders of magnitude lower mobilities in both CTLs, obtaining the same efficiency trends as a function of ΔE_C as those of Figure 10. We also neglected tunneling-enhanced recombination, which could increase interface recombination in both the ionic and pin solar cell. Further simulations will investigate this phenomenon. Regarding the ion contents, we recall that our results assume either a very high or negligible concentration of mobile ions. Intermediate behaviors to those observed throughout this section are obtained when ion concentrations are between both extremes. Moreover, although the adopted numerical model assumes one mobile and one fixed ion concentration, we expect the same trends found here if both ion species are mobile, as a second mobile species only delivers a higher degree of symmetry of the electrostatic landscape in the absorber.

All results shown in this contribution correspond to steady-state conditions, focusing on device performance under typical solar operation conditions. Therefore, the conclusions drawn from our results are not to be extended to transient behavior. For instance, at $\Delta E_C = -0.5$ eV the $J(V)$ curve of the ionic cell with bulk recombination shows no kink (cf. Figure 11, $\Delta E_C = -0.5$ eV) in steady state, however it appears in transient simulations where the scan rate is sufficiently high as to impede the ions to compensate the instantaneous electric field.

5. Conclusions

According to the simulations presented in this work, the presence of mobile ions in the absorber of a solar cell does not necessarily imply lower energy conversion efficiency. Moreover, we find that depending on the dominating recombination location (i.e., bulk or interfaces), solar cells with a high mobile ion concentration (here termed ionic cells) may reach higher efficiencies than ion-free (or pin) cells.

Focusing on the incidence of interfacial energy band offsets on solar output, our results show that pin solar cells require the smallest possible band offsets (maximizing built-in voltage), reducing energy losses for collected carriers. This is interpreted in terms of traditional solar cell knowledge, where high built-in voltage warrants high photocarrier collection at higher bias, ensuring high fill factors. If carrier mobilities are sufficiently high, slightly negative offsets (down to -0.1 eV) are also admissible without compromising photocarrier collection. In ionic solar cells, however, there is no a priori choice for band offsets that enables the highest efficiency: the optimum offsets depend on the location of dominating recombination. In the case of dominating bulk recombination, the efficiency is increased by choosing unequal band offsets $\Delta E_C \neq \Delta E_V$, in order to avoid high symmetry concentrations that lead to high injection conditions. In the case of dominating interface recombination, the band offset at the interface with strongest interface recombination is to be minimized, in agreement with experiments in metalorganic PVK solar cells with fullerene ETLs.[5] However, this may not be a generally applicable strategy, since in practice, the choice of CTLs is subject to additional criteria regarding fabrication possibilities, interface chemistry, thermal parameters, and optical criteria (e.g., refraction index optimization). Therefore, we highlight a work-around strategy emerged from our simulations: if a

non-negligible band offset is unavoidable at the interface with strongest recombination, we require increasing the band offset at the opposite interface. According to our results, this route still enables efficiencies well over 20%, assuming state-of-the-art material parameters. The seemingly counter-intuitive solution of requiring a band offset increase is resolved by noticing that higher offsets introduce an asymmetry in carrier concentration, driving the ionic solar cell farther away from high injection conditions, therefore reducing recombination. This is only possible in the ionic solar cell, where the band bendings caused by the accumulation of ions at the interfaces allow carriers from the CTLs to conform majority carrier concentrations in the absorber. Whether this is the case of recent compelling experiments where higher-band offsets delivered higher efficiencies in PVK solar cells,[22] is to be determined by further experimental evidence.

Supporting Information

Supporting Information is available from the Wiley Online Library or from the author.

Conflict of Interest

The authors declare no conflict of interest.

Data Availability Statement

The data that support the findings of this study are available from the corresponding author upon reasonable request.

Keywords

band alignments, band offsets, interface recombination, mobile ions, perovskite solar cells

[1] Y. Cheng, Y. Peng, A. K.-Y. Jen, H.-L. Yip, *Sol. RRL* **2022** 6, 2100545.
[2] M. A. Green, E. D. Dunlop, G. Siefer, M. Yoshita, N. Kopidakis, K. Bothe, X. Hao, *Prog. Photovolt.: Res. Appl.* **2023**, *31*, 3.
[3] H. Zhou, Q. Chen, G. Li, S. Luo, T-b. Song, H.-S. Duan, Z. Hong, J. You, Y. Liu, Y. Yang, *Science* **2014**, *345*, 542.
[4] C. M. Wolff, F. Zu, A. Paulke, L. P. Toro, N. Koch, D. Neher, *Adv. Mater.* **2017**, *29*, 28.
[5] J. Haddad, B. Krogmeier, B. Klingebiel, L. Krückemeier, S. Melhem, Z. Liu, J. Hüpkes, S. Mathur, T. Kirchartz, *Adv. Mater. Interfaces* **2020**, *7*, 2000366.
[6] F. H. Isikgor, S. Zhumagali, L. V. T. Merino, M. De Bastiani, I. Mcculloch, S. De Wolf, *Nat. Rev. Mater.* **2023**, *8*, 89.
[7] P. Schulz, E. Edri, S. Kirmayer, G. Hodes, D. Cahen, A. Kahn, *Energy Environ. Sci.* **2014**, *7*, 1377.
[8] S. Wang, T. Sakurai, W. Wen, Y. Qi, *Adv. Mater. Interfaces*, **2018**, *5*, 1800260.
[9] D. Li, L. Chao, C. Chen, X. Ran, Y. Wang, T. Niu, S. Lv, H. Wu, Y. Xia, C. Ran, L. Song, S. Chen, Y. Chen, W. Huang, *Nano Lett.* **2020**, *20*, 5799.

[10] M. Stolterfoht, P. Caprioglio, C. M. Wolff, J. A. Márquez, J. Nordmann, S. Zhang, D. Rothhardt, U. Hörmann, Y. Amir, A. Redinger, L. Kegelmann, F. Zu, S. Albrecht, N. Koch, T. Kirchartz, M. Saliba, T. Unold, D. Neher, *Energy Environ. Sci.* **2019**, *12*, 2778.
[11] S. Shao, M. A. Loi, *Adv. Mater. Interfaces*, **2020**, *7*, 1901469.
[12] W. Wang, Z. Su, B. Sun, L. Tao, H. Gu, H. Wui, Q. Wei, W. Shi, X. Gao, Y. Xia, Y. Chen, *Adv. Mater. Interfaces*, **2021**, *8*, 2001683.
[13] Z. Liu, J. Siekmann, B. Klingebiel, U. Rau, T. Kirchartz, *Adv. Energy Mater.* **2021**, *11*, 2003386.
[14] G. Xu, R. Xue, S. J. Stuard, H. Ade, C. Zhang, J. Yao, Y. Li, Y. Li, *Adv. Mater.* **2021**, *33*, 2006753.
[15] P. Schulz, D. Cahen, A. Kahn, *Chem. Rev.* **2019**, *119*, 3349.
[16] E. M. Hutter, T. Kirchartz, B. Ehrler, D. Cahen, E. Von Hauff, *Appl. Phys. Lett.* **2020**, *116*, 100501.
[17] G. M. Arumugam, S. K. Karunakaran, C. Liu, C. Zhang, F. Guo, S. Wu, Y. Mai, *Nano Select* **2021**, *2*, 1081.
[18] K. Wang, S. Olthof, W. S. Subhani, X. Jiang, Y. Cao, L. Duan, H. Wang, M. Du, S (Frank). Liu, *Nano Energy* **2020**, *68*, 104289.
[19] A. Raj, M. Kumar, A. Anshul, *Mater. Today Chem.* **2021**, *22*, 100595.
[20] P. Basumatary, P. Agarwal, *Mater. Res. Bull.* **2022**, *149*, 111700.
[21] J. Siekmann, A. Kulkarni, S. Akel, B. Klingebiel, M. Saliba, U. Rau, T. Kirchartz (Preprint), *arXiv:2302.05749, v1*, submitted: Feb. **2023**.
[22] Q. Wang, F. Zu, P. Caprioglio, C. M. Wolff, M. Stolterfoht, M. Li, S.-H. Turren-Cruz, N. Koch, D. Neher, A. Abate, *ACS Energy Lett.* **2020**, *5*, 2343.
[23] Z. Safari, M. B. Zarandi, A. Giuri, F. Bisconti, S. Carallo, A. Listorti, C. Esposito Corcione, M. R. Nateghi, A. Rizzo, S. Colella, *Nanomaterials* **2019**, *9*, 1627.
[24] N. Tessler, Y. Vaynzof, *ACS Energy Lett.* **2020**, *5*, 1260.
[25] N. Mozaffari, D. Walter, T. P. White, A. D. Bui, G. D. Tabi, K. Weber, K. R. Catchpole, *Sol. RRL* **2022**, *6*, 2101087.
[26] M. García-Rosell, A. Bou, J. A. Jiménez-Tejada, J. Bisquert, P. Lopez-Varo, *J. Phys. Chem. C* **2018**, *122*, 13920.
[27] A. Pockett, M. J. Carnie, *ACS Energy Lett.* **2017**, *2*, 1683.
[28] R. A. Belisle, W. H. Nguyen, A. R. Bowring, P. Calado, X. Li, S. J. C. Irvine, M. D. Mcgehee, P. R. F. Barnes, B. C. O'regan, *Energy Environ. Sci.* **2017**, *10*, 192.
[29] N. E. Courtier, *Phys. Rev. Appl.* **2020**, *14*, 024031.
[30] N. E. Courtier, J. M. Foster, S. E. J. O'kane, A. B. Walker, G. Richardson, *Eur. J. Appl. Math.* **2019**, *30*, 427.
[31] Except for e.g., TiO$_2$, see M. Dou, C. Persson, *J. Appl. Phys.* **2013**, *113*, 083703.
[32] J. N. Wilson, J. M. Frost, S. K. Wallace, A. Walsh, *APL Mater.* **2019**, *7*, 010901.
[33] T. Markvart, *IEEE J. Photovolt.* **2019**, *9*, 1614.
[34] U. Rau, G. Kron, J. H. Werner, *J. Phys. Chem. B* **2003**, *107*, 13547.
[35] M. A. Green, in *Solar Cells: Operating Principles, Technology, And System Applications* Prentice-Hall, Inc., Englewood Cliffs, NJ **1982**.
[36] J. Nelson, in *The Physics Of Solar Cells*, Imperial College Press, London, UK **2003**.
[37] J. Hüpkes, U. Rau, T. Kirchartz, *Sol. RRL* **2022**, *6*, 2100720.
[38] S. M. Sze, K. K. Ng, in *Physics of Semiconductor Devices*, John Wiley & Sons, Hoboken, NJ **2006**.
[39] N. E. Courtier, J. M. Cave, A. B. Walker, G. Richardson, J. M. Foster, *J. Comput. Electron.* **2019**, *18*, 1435.
[40] N. Mozaffari, D. Walter, T. P. White, A. D. Bui, G. D. Tabi, K. Weber, K. R. Catchpole, *Sol. RRL* **2022** 6, 2101087.
[41] C. Eames, J. M. Frost, P. R. F. Barnes, B. C. O'Regan, A. Walsh, M. S. Islam, *Nat. Commun.* **2015**, *6*, 7497.
[42] Notice that we use the effective lifetime in order to include radiative recombination, which is not negligible at the extreme values of band offsets adopted here.

[43] The observed difference between the simulated electron concentration and the analytical value originates in the expression for the Debye charge becoming less accurate when the ETL starts to show electron depletion, as in the case with $-0.1\,eV$ band offset.

[44] S. Rühle, *Sol. Energy* **2016**, *130*, 139.

[45] In case of very high recombination, the open-circuit voltage is smaller than the built-in voltage for any band offset, so the band bendings stay always positive.

[46] W. Li, M. Uller. Rothmann, A. Liu, Z. Wang, Y. Zhang, A. R. Pascoe, J. Lu, L. Jiang, Y. Chen, F. Huang, Y. Peng, Q. Bao, J. Etheridge, U. Bach, Y-B. Cheng, *Adv. Energy Mater.* **2017**, *7*, 1700946.